Materials and Interfaces

Article

Magnetic Assembly of Nonuniform Nanocrystal Clusters into Responsive Photonic Crystals

Fenglian Qi [1,2], Qingsong Fan [2], Chaolumen Wu [2], and Yadong Yin [2,*]

[1] College of Chemistry and Molecular Engineering, Qingdao University of Science and Technology, Qingdao 266042, China
[2] Department of Chemistry, University of California, Riverside, CA 92521, USA
* Correspondence: yadong.yin@ucr.edu

Received: 5 December 2025; Revised: 23 December 2025; Accepted: 25 December 2025; Published: 26 December 2025

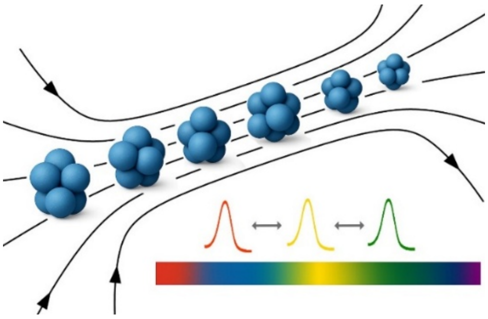

Abstract: Colloidal assembly of photonic crystals typically relies on uniform building blocks to achieve the required periodicity. However, the difficulties in large-scale production of uniform particles limit the practical use of colloidal photonic crystals in many exciting applications. Here, we show that this uniformity requirement can be relaxed by increasing the interparticle spacing during colloidal magnetic assembly, enabling the formation of responsive photonic crystals from particles with a broader size range. Specifically, we demonstrate that magnetite nanocrystal clusters with a wide size range of 40–60 nm, formed by breaking their large aggregates via ultrasonication in the presence of polymeric ligands, can be magnetically assembled in solution into one-dimensional photonic crystals with tunable optical diffraction across the entire visible spectrum. The strong electrostatic repulsion imparted by the polymeric ligands results in large interparticle separation, reducing the negative impact of low particle uniformity and enabling the required periodicity for notable diffraction and broad spectral tunability.

Keywords: nonuniformity; nanocrystal clusters; magnetic assembly; one-dimensional; photonic crystals; poly(acrylic acid)

1. Introduction

Photonic crystals are functional materials with periodically modulated refractive indices [1–3]. Their strong interaction with light induces constructive and destructive interference, producing optical diffraction that is determined by the crystals' order and periodicity [4]. Conventional methods for preparing colloidal photonic crystals rely on uniform building blocks of appropriate sizes to achieve bright structural colors and tunable optical diffraction [5]. As determined by Bragg's law, colloidal particles with uniform sizes in the range from 150 to 300 nm are commonly employed as ideal building blocks for preparing close-packed crystals with diffraction in the visible range [6–9]. Various materials, such as SiO_2 [6,10], polymers [11–13], and polysulfide [5], have been prepared as uniform colloidal spheres for photonic crystal assembly. Besides particle size, the refractive indices of materials also contribute to determining the diffraction wavelength. For materials with low refractive indices, such as SiO_2, a particle diameter of 200–300 nm is required to produce visible diffraction [14]. This contrasts with materials like CeO_2, which have higher refractive indices and can produce visible responses with particles as small as 125 nm [15].

For non-close-packed photonic crystals, the building-block size can be reduced further to below 100 nm due to interparticle separations. Earlier research by Asher et al. demonstrated that highly charged polystyrene beads of 110 and 120 nm could self-assemble into crystalline colloidal arrays [16,17], relying on electrostatic repulsion to maintain structural order. Another example involves the magnetic assembly of superparamagnetic nanocrystal clusters of magnetite (Fe_3O_4), first developed in our group [18,19] and then followed by several other groups [20,21]. In these cases, strong electrostatic repulsion could create large interparticle separations, enabling small particles to be assembled into one-dimensional (1D) arrays with bright, magnetically responsive structural colors.

This work aims to highlight another key benefit of the magnetic assembly approach for forming non-close-packed structures: reducing the negative impact of nonuniformity in the building blocks. We show that large separations induced by strong electrostatic repulsion can offset the effects of particle-size polydispersity, enabling the formation of the periodicity required for optical diffraction. Starting with bulk aggregates of Fe_3O_4 nanocrystals produced via solvothermal processing, we found that ultrasonication could break them into nanocrystal clusters of 40–60 nm. Despite their low size uniformity, these clusters could still be assembled in aqueous solution into 1D arrays with magnetically responsive structural colors of notable brightness. Polyacrylic acid (PAA) was used as a capping ligand during ultrasonication to stabilize nanocrystal clusters formed from aggregate breakage and to promote strong electrostatic repulsion during magnetic assembly. Since the initial solvothermal synthesis of bulk nanocrystal aggregates is easily scalable, their convenient transformation into nanocrystal clusters, combined with the high tolerance to nonuniformity of the magnetic assembly process, makes this approach promising for applications that require large amounts of material over wide areas, while maximum brightness in structural color isn't essential.

2. Experimental Section

2.1 Materials

$FeCl_3 \cdot 6H_2O$, sodium formate, polyvinylpyrrolidone (PVP, M_w. 40,000), PAA (M_w. 1800), EG, PG, resorcinol, and formaldehyde solution (37 wt % in water) were purchased from Sigma-Aldrich (St. Louis, MI, USA). $NH_3 \cdot H_2O$ was purchased from Fisher (Pittsburgh, PL, USA). All chemicals were used as received without further purification.

2.2 Synthesis of PAA-Modified Magnetic Clusters

Magnetic clusters were prepared using a modified solvothermal polyol method [22]. $FeCl_3 \cdot 6H_2O$ (16 mmol), sodium formate (29 mmol), and PVP (2.0 g) were dissolved in a mixture of ethylene glycol (35 mL) and 1,2-propylene glycol (5 mL) under vigorous stirring. The solution was sealed in a 100 mL Teflon-lined stainless-steel autoclave and heated at 210 °C for 8 h. After cooling to room temperature overnight, the black product was collected by centrifugation and washed three times with water. The resulting material was re-dispersed in 50 mL of water, followed by the addition of 10 mL of PAA solution (7.2 mg/mL). The mixture was sonicated for 30 min, washed three times with water, and separated overnight using a magnet. Finally, the clusters were re-dispersed in 30 mL of water.

2.3 Centrifugal Separation of PAA-Modified Magnetic Clusters

Four representative samples of PAA-modified magnetic clusters were obtained through sequential centrifugation. Prior to separation, the dispersion was sonicated for 20 min. The first fraction (M1) was collected from the supernatant after centrifugation at 11,000 rpm for 3 min. The remaining precipitate was re-dispersed in 30 mL of water by ultrasonication, and subsequent fractions (M2, M3, and M4) were obtained by centrifugation at 9000, 7000, and 5000 rpm for 3 min, respectively. All samples were then concentrated to 10 mg/mL in water for further characterization.

2.4 Fixation of 1D Assemblies of Nanocrystal Clusters

1D assemblies were stabilized using a conformal coating of phenolic resin with slight modifications to the reported procedure [23]. Two precursor solutions were prepared separately: one by dissolving 5 mg of resorcinol in 1 mL of water, and the other by mixing 7 μL of formaldehyde (37 wt % in water) with 293 μL of water. Subsequently, 30 μL of resorcinol solution and 9 μL of diluted formaldehyde solution were combined with 100 μL of sample M1 (≈0.8 mg/mL) in a well of a 96-well plate. After ultrasonication for 3 min, the mixture was placed under a parallel magnetic field by positioning it adjacent to a neodymium magnet (25 mm × 25 mm × 9 mm, ≈2020 G) for 5 min. Then, 13 μL of $NH_3 \cdot H_2O$ (0.28%) was added slowly without disturbing the system, and the reaction continued for an additional 20 min under the same field. Following completion, the magnetic chains were separated from the solution using a magnetic field and then redispersed in 50 μL of water. The M2-based nanocluster chains were fixed using the same method and conditions as described above. The M3-based nanocluster chains were fixed with the same method, but the distance between the sample and the magnet was adjusted to 0.85 cm (magnetic strength: ca. 1380 Gauss). The M4-based nanocluster chains were fixed using the same method, with the M4 sample concentration reduced to 0.4 mg/mL and the distance between the sample and the magnet increased to 3.20 cm (magnetic strength: ca. 490 Gauss).

2.5 Sample Characterization

Dark-field optical images were obtained using a Zeiss AXIO Imager microscope (Oberkochen, Germany). SEM images of PAA-modified magnetic clusters were captured with a Zeiss G300 scanning electron microscope, and TEM images were recorded on a Tecnai T12 transmission electron microscope operating at 120 kV. Dynamic light scattering (DLS) and zeta potential measurements were performed using a Delsa NanoC Particle Analyzer and Zeta-Potential Analyzer (Beckman Coulter, Brea, CA, USA), respectively. Magnetic properties were characterized with a MicroMag 3900 Series (Lake Shore, Westerville, OH, USA) vibrating sample magnetometer under applied fields ranging from −20 to 20 kOe at 298 K. Reflection spectra were collected using an Ocean Optics HR2000 CG-UV-NIR spectrometer coupled with a six-around-one reflection probe, with incident and reflection angles fixed at 0° and the magnetic field oriented parallel to the incident light. Structural colors of photonic crystals were documented using a digital camera under the same magnetic field alignment.

3. Results and Discussion

Fe_3O_4 nanocrystal clusters were synthesized via a solvothermal process [22]. Ethylene glycol (EG) and 1,2-propylene glycol (PG) were employed as both the solvents and reducing agents during the reaction. In the presence of sodium formate, ferric ions were first hydrolyzed to form ferric hydroxide precipitates, which were then reduced to Fe_3O_4 nanocrystals by EG and PG at high temperature [22]. Due to the absence of capping ligands, the initial product appeared as bulk aggregates that quickly settled from the solution, as shown in the optical microscopy image and photo in Figure 1a. Ultrasonication of the aqueous solution containing these aggregates and PAA produced a colloidal dispersion of nanocrystal clusters [20,24]. During this process, PAA binds to the surface of the magnetic clusters through strong coordination between its carboxylate groups and the iron ions on the nanocrystal surface. As discussed later, it also provides large surface charges, resulting in strong electrostatic repulsion between the clusters [25]. As shown in Figure 1b, large aggregates disappeared after ultrasonication, confirming their effective breakage into small nanocrystal clusters, which also exhibited greatly improved colloidal stability compared to their original aggregate form. The scanning electron microscopy (SEM) image in Figure 1c shows their quasi-spherical shape with an average size below 100 nm. The transmission electron microscopy (TEM) image in Figure 1d indicates individual nanocrystals with an average size of around 20 nm, although it is difficult to distinguish between clusters when they are connected.

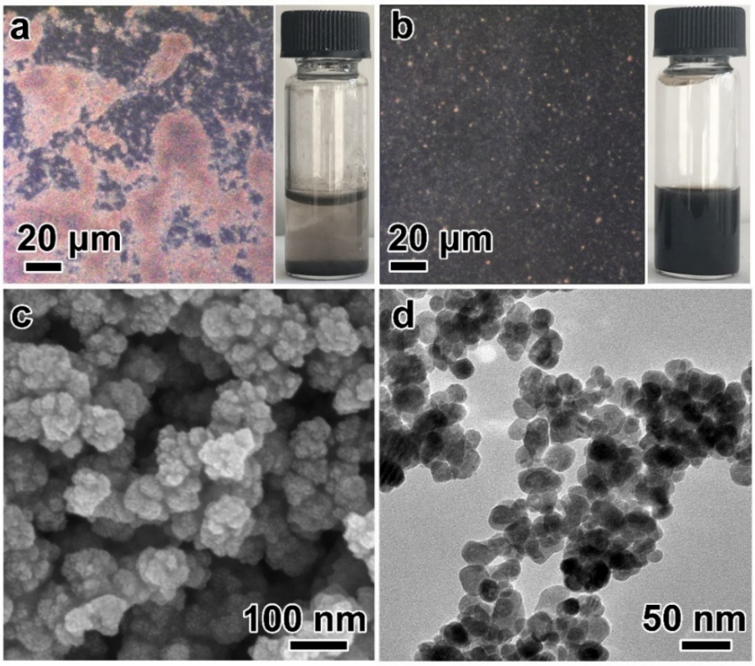

Figure 1. (**a**) Dark-field optical microscopy image of Fe_3O_4 nanocrystal aggregates synthesized via a solvothermal process, with the inset photo showing the sample in water; (**b**) Dark-field optical microscopy image of nanocrystal clusters formed after sonicating the aqueous mixture of aggregates and PAA, with the inset photo showing the particle dispersion after sitting for 30 min; (**c**,**d**) SEM image (**c**) and TEM image (**d**) of the PAA-modified nanocrystal clusters.

While effective at breaking nanocrystal aggregates, ultrasonication has limited capability to control cluster sizes. To obtain distinct structural colors, centrifugation-based size selection was performed by collecting nanocrystal clusters that remained in the supernatant after centrifugation at a specific speed. Specifically, four samples, M1, M2, M3, and M4, were collected from the supernatants after the initial product was centrifuged at 11,000, 9000, 7000, and 5000 rpm, respectively. Dynamic light scattering (DLS) study (Figure 2a,b) shows that the cluster sizes increase gradually from 83 nm (M1) to 104 nm (M2), 115 nm (M3), and finally 136 nm (M4). Their measured polydispersity indices (PDIs), which define the breadth of size distribution, range from 0.06 to 0.10 (Figure 2b), indicating relatively broad size distribution as compared with near-monodisperse spheres (e.g., PDI = 0.016) used in preparing conventional close-packed photonic crystals [5] or uniform magnetite nanocrystal clusters prepared in our previous work [18].

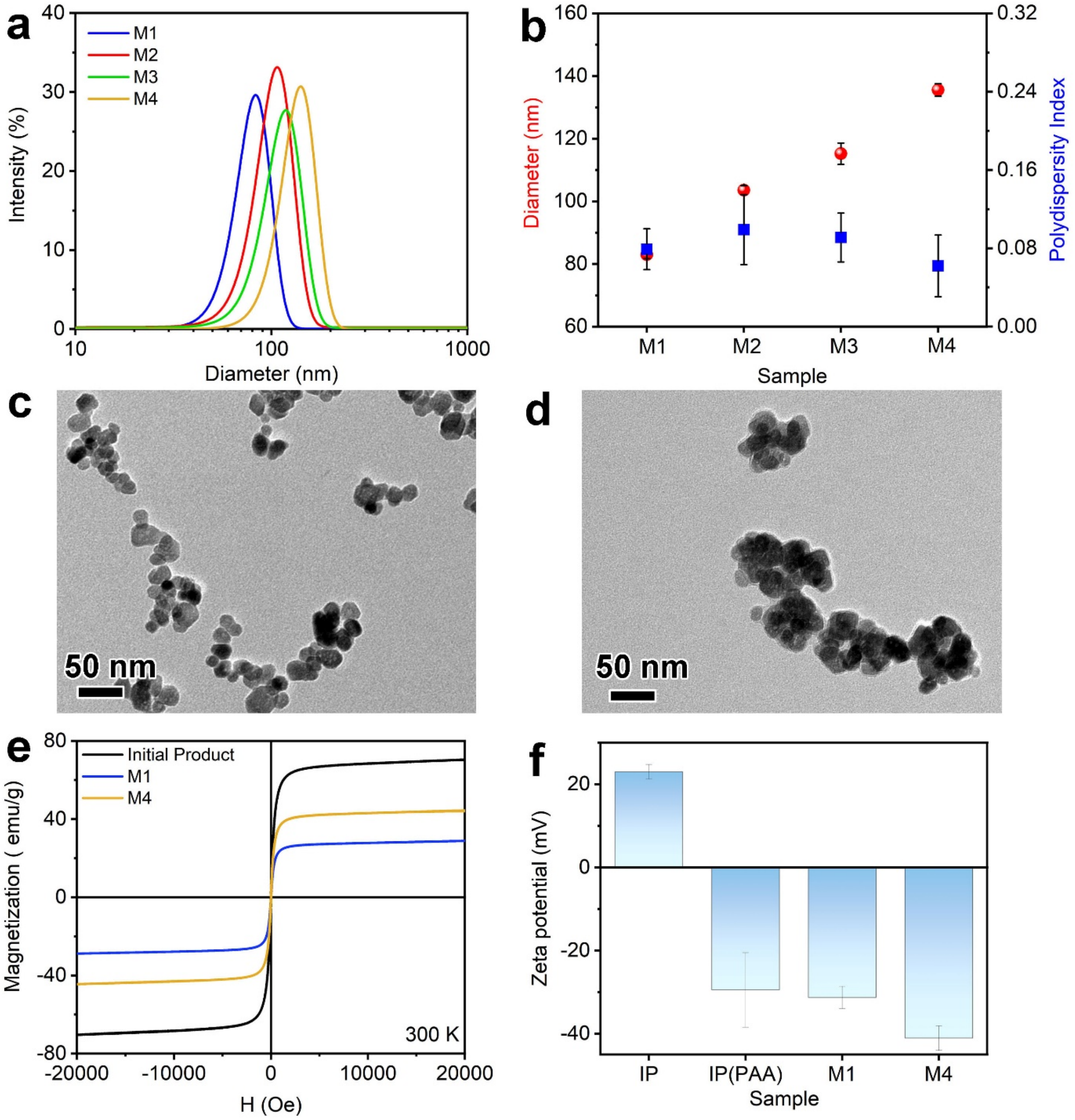

Figure 2. (**a**,**b**) DLS measurement of samples M1, M2, M3 and M4: size distribution (**a**) and corresponding diameter and PDI (**b**); (**c**,**d**) TEM images of samples M1 (**c**) and M4 (**d**); (**e**) Magnetic hysteresis loops of the initial nanocrystal aggregates and samples M1 and M4; (**f**) ζ-potential values of the initial product of nanocrystal aggregates (IP), PAA-modified cluster before size selection (IP(PAA)), and samples M1 and M4.

Using the smallest (M1) and largest (M4) magnetic clusters as examples, we systematically studied their morphologies and magnetically responsive optical properties. The TEM images in Figure 2c,d demonstrate the nonuniform size and irregular shape of the clusters, with M1 size below 50 nm and M4 ~60 nm. The size discrepancies between TEM and DLS measurements are expected, as TEM measures the physical size of clusters in a dry state, while DLS measures the hydrodynamic diameter, which includes contributions from the solvent layer around the particles, surface ligands, and the diffuse ionic layer. Due to their small grain sizes, these clusters are superparamagnetic. The hysteresis curves in Figure 2e suggest superparamagnetic behavior, with coercivities of 24, 16, and 19 Oe for the initial aggregates, sample M1, and sample M4, respectively, which are smaller than the typical superparamagnetic limit of 30 Oe [24,25]. Moreover, the saturation magnetization is 29 emu/g for sample M1 and 44 emu/g for sample M4 at room temperature, in good agreement with the average particle size observed in Figure 2c,d [25]. The lower saturation magnetization of M1 and M4 than that of the initial aggregates (70 emu/g) is attributed to the contribution of PAA to the sample mass and to reduced domain interactions within the clusters.

Modification of the nanocrystal clusters with PAA confers negative surface charges, as shown by the ζ-potential measurements in Figure 2f. Before PAA modification, the ζ-potential of the initial aggregates was +23 mV, likely due to surface-bound iron ions. After modification, the ζ-potential shifted to −29 mV because of the abundant negative charges carried by carboxylate groups. At a pH near 7, PAA's carboxyl groups are significantly deprotonated, thanks to its pK_a of ~4.5 [26,27], which provides the nanocrystal surface with negative charges. These negative surface charges remained after size selection, with a ζ-potential of −31 mV for sample M1 and −41 mV for sample M4. The differences in ζ-potential between M1 and M4 may result from the differences in cluster size and the number of primary nanocrystals within. For smaller clusters, neighboring ligands are closer to each other and therefore experience more electrostatic repulsion, leading to a lower overall ligand density. A smaller number of primary nanocrystals in a cluster may also decrease surface complexity, allowing fewer ligands to bind.

The 1D assembly of magnetic clusters under magnetic fields was verified by coating the assembled structures with a resorcinol-formaldehyde resin via a sol-gel-like process in water [28,29]. The phenolic resin was used, instead of silica in our previous study, to avoid the need for ethanol as a solvent [19,30,31], which tends to cause severe aggregation of the current magnetic clusters. Further, we applied a strong magnetic field during coating to mitigate the challenges posed by the large separations within the assemblies.

The phenolic resin fixation of samples M1, M2, M3, and M4 was performed under 2020 G, 2020 G, 1380 G, and 490 G of magnetic fields, respectively. Figure 3a–d clearly confirmed the 1D periodic configurations of the magnetic nanoclusters. After the addition of phenolic resin precursor, the diffraction of the assemblies blueshifted owing to the increase in ionic strength (Figure S1). Relatively strong magnetic fields were applied to all four samples to decrease the inter-cluster spacings, making it easier to encapsulate the entire chains. Figure 3e further shows the electron tomography TEM images of a 1D chain assembled from sample M4, taken by rotating the chain from -45° to 45° counterclockwise along its long axis. Distinct gaps between neighboring nanocrystal clusters can be observed, indicating that the chain is assembled from discrete clusters rather than a continuous aggregation of individual nanocrystals. Treating individual nanocrystals as spheres, 20 nm in diameter as estimated from Figure 1d, allows us to estimate the average cluster size and the number of nanocrystals within each cluster. As summarized in Figure 3f, the average size of clusters increases from 40 nm (M1) to 53 nm (M2), 56 nm (M3), and finally 60 nm (M4), with the average number of nanocrystals in each cluster increasing from 2 to 5, 7, and 9, respectively. We further constructed a simple model (Figure 3g) to help illustrate the number of nanocrystals and their configuration within magnetic clusters of varying sizes.

Although the nanocrystal clusters were nonuniform in size and irregular in shape, we still observed tunable structural colors when their dispersions were exposed to magnetic fields. Figure 4a shows photos of the four samples in round glass vials (10 mg/mL) captured from the front direction, under a magnetic field aligned at the same angle (Figure S2). When the magnetic field decreases from 2020 G to 200 G, the structural color of sample M1 shifts from purple to green due to increased interparticle spacing. When the field is further reduced to 180 G, the color returns to its original grey, due to the disassembly of photonic chains under such a weak magnetic field. Similar trends in structural color changes are seen in samples M2, M3, and M4. At the same magnetic field strength, the structural color redshifts as the cluster size increases from M1 to M4. Smaller clusters, especially M1, diffract only short-wavelength light, from ~414 nm to 584 nm, with relatively weak, broad peaks (Figure 4b). Larger clusters exhibit higher diffraction intensity and a broader tuning range, primarily due to stronger magnetic interactions and larger scattering cross-sections [19]. Notably, M4 displays a much brighter structural color compared to the other samples, demonstrating wide spectral tuning of optical diffraction in the visible range, from 540 nm to 652 nm (Figure 4c). To compare the diffraction positions and intensities of the four samples, their reflection spectra under a magnetic field of 490 G are shown in Figure 4d. As the cluster size increases from 40 nm (M1) to 60 nm (M4), the peaks shift from 443 nm to 553 nm, respectively. The correlation between peak position and sample size is summarized in Figure 4e. When decreasing the magnetic field strength from 2020 G to 490 G by increasing the sample-magnet distance, we observed an initial slow and then rapid redshift in the diffraction peaks for all four samples.

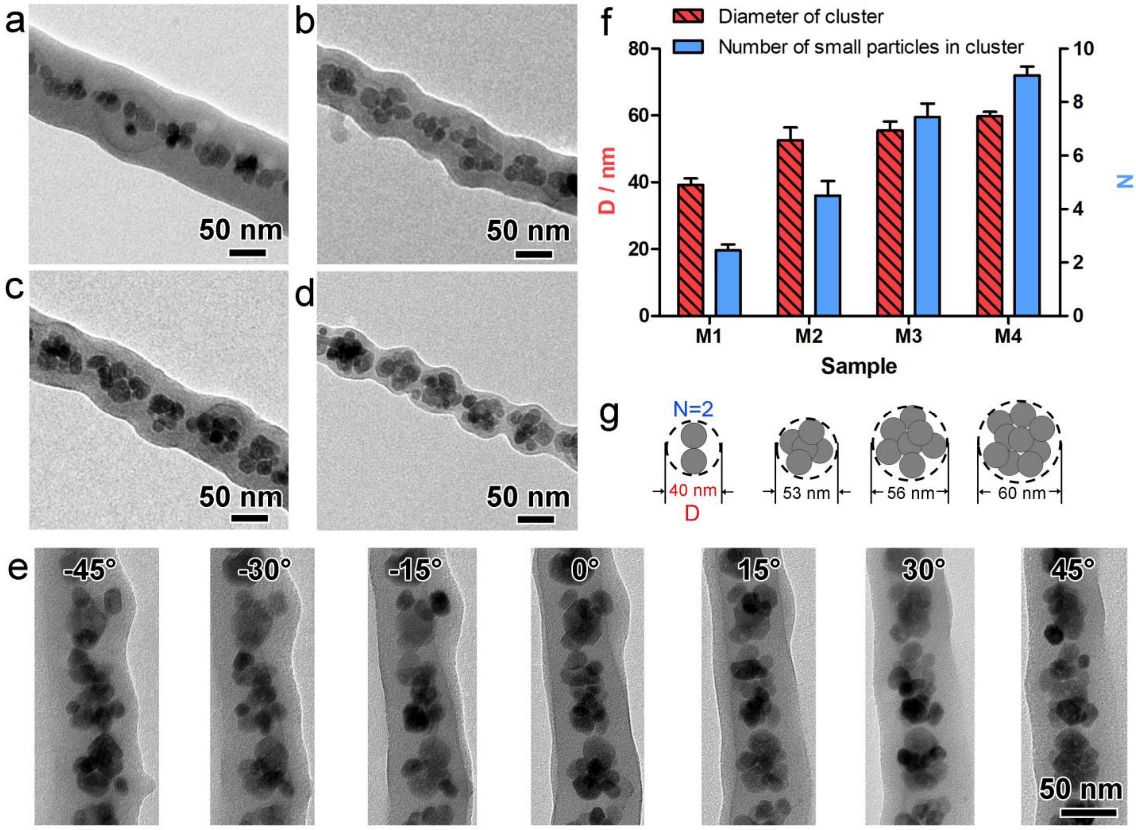

Figure 3. (**a**–**d**) TEM images of the magnetic assemblies of nanocrystal clusters of samples M1 (**a**), M2 (**b**), M3 (**c**), and M4 (**d**), all fixed by a phenolic resin coating; (**e**) Electron tomography images of a fixed M4 chain rotated along its long axis for various angles; (**f**) Estimated mean diameter of the magnetic clusters and the number of contained nanocrystals; (**g**) Scheme illustrating the configuration in nanocrystal clusters, from left to right: M1, M2, M3, and M4.

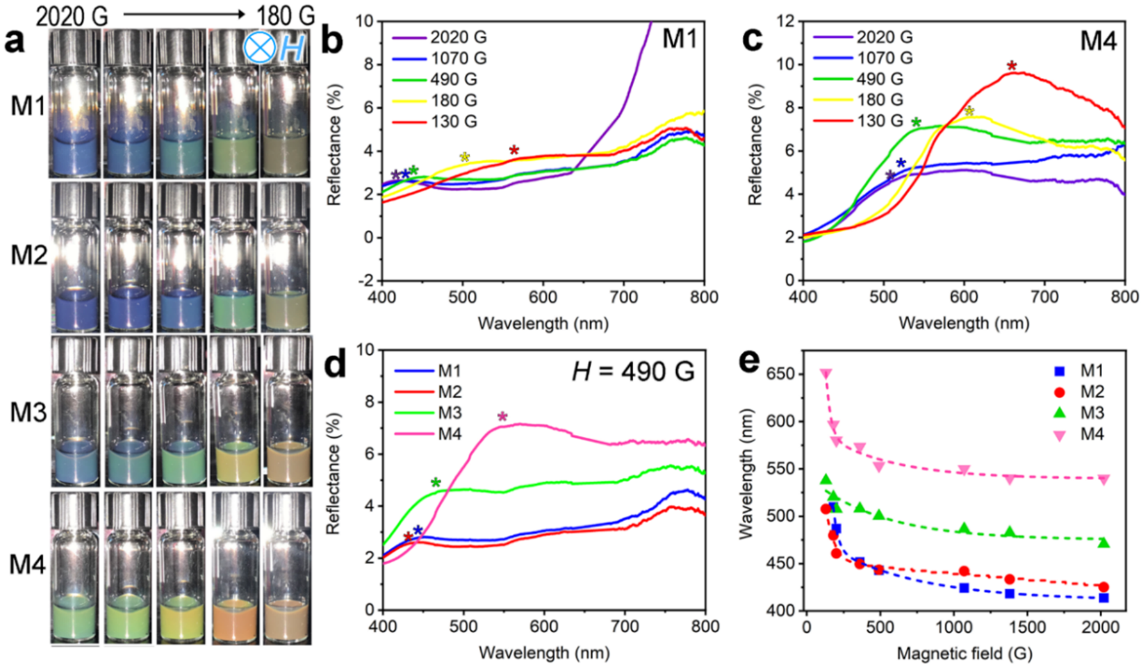

Figure 4. (**a**) Photographs of samples M1, M2, M3, and M4 under varying magnetic fields; (**b**,**c**) Reflection spectra of samples M1 (**b**) and M4 (**c**) under different magnetic fields; (**d**) Reflection spectra of all four samples at a magnetic field of 490 G; (**e**) Change in peak position with magnetic field strength. The concentration of each sample is 10 mg/mL. The symbol '*' in figures b–d indicates the position of the main reflection peaks.

We further optimized the concentration of sample M4 to enable full-range optical diffraction tuning. An increase in sample concentration results in a blueshift in diffraction and improved response at lower field strengths, broadening the range of structural color changes (Figure S3). At 20 mg/mL, the reflection spectra show a peak shift from 470 nm to 663 nm as the magnetic field decreases from 2020 G to 60 G, accompanied by a color transition from blue to red (Figure 5a). Unlike our previous work where uniform magnetic particles of similar size produced only blue light [18], the broad size distribution of magnetic clusters in this study allows for a significantly wider tuning range [19].

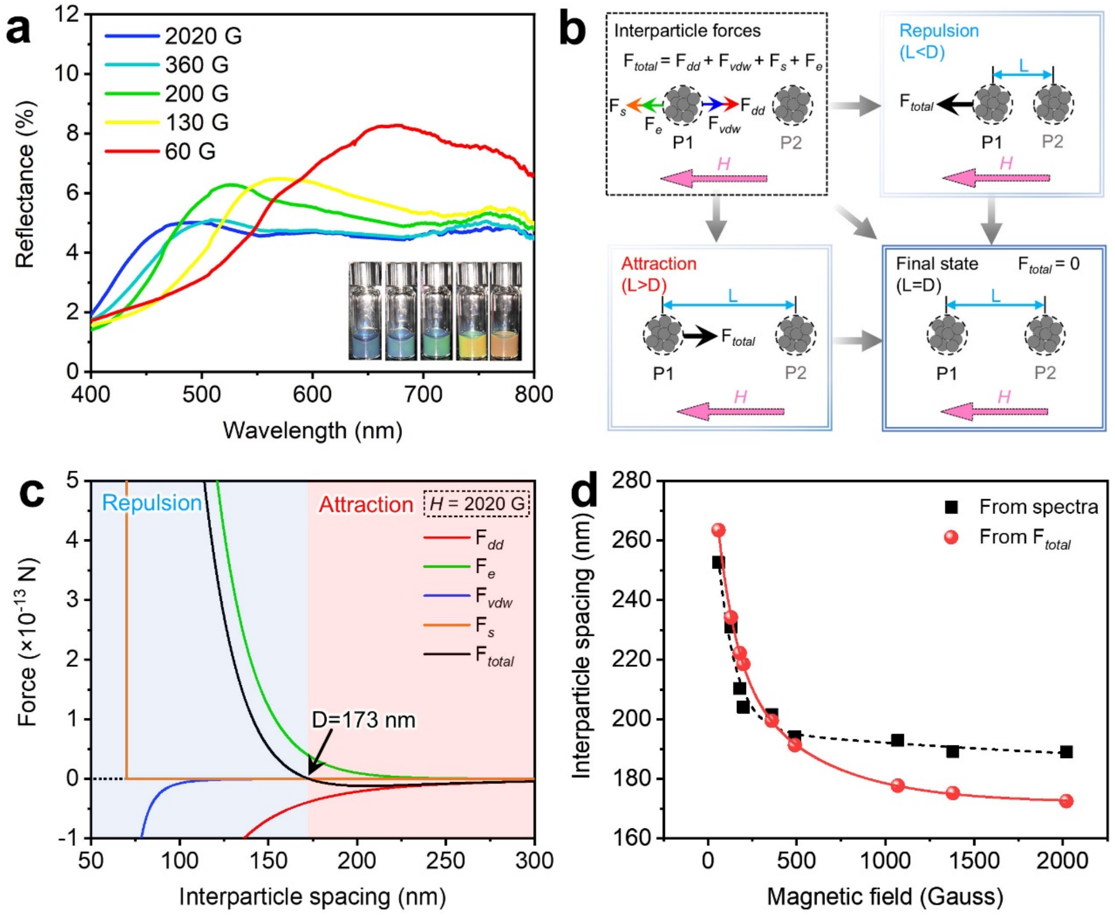

Figure 5. (**a**) Reflection spectra and corresponding color changes of sample M4 (20 mg/mL) under varying magnetic fields; (**b**) Schematic of positional adjustment of the magnetic clusters driven by interparticle forces during magnetic assembly, with the pink arrows indicating the direction of magnetic fields; (**c**) Simulated force profile at 2020 G as interparticle spacing varies; (**d**) Comparison of spacing derived from spectral data (black) and force equilibrium calculations (red) across magnetic field strengths.

To investigate the periodicity and driving forces behind photonic crystal formation with small clusters, we calculated the interparticle spacing of sample M4 (10 mg/mL) using Bragg's law and force dynamics analysis. Based on Figure 3f,g, each cluster is modeled as a 60-nm sphere comprising nine 20-nm magnetic nanocrystals. In addition to Bragg's law [32], we analyzed the forces governing equilibrium spacing between adjacent clusters. As shown in Figure 5b, four interactions were considered: magnetic dipole–dipole attraction ($\vec{F}_{dd}$), van der Waals forces ($\vec{F}_{vdw}$), electrostatic repulsion ($\vec{F}_e$), and steric repulsion($\vec{F}_s$). Under a uniform magnetic field, the dipole moment ($\vec{m}$) of a cluster is given by $\vec{m} = \chi \vec{H} V$, where χ is the volume magnetic susceptibility, $\vec{H}$ the applied field, and V the cluster volume. In the 1D photonic arrays as shown in Figure 3d, the dipole-dipole attractive interaction between two clusters with an interparticle spacing of d_{12} can be described as: $\vec{F}_{dd} = -\nabla U_{dd}$ [33], where U_{dd} is the dipole-dipole potential that can be calculated by $U_{dd,12} = -\frac{\mu_{water}}{4\pi}\left(\frac{3(\vec{m}_1 \cdot \vec{d}_{12})(\vec{m}_2 \cdot \vec{d}_{12})}{d_{12}^5} - \frac{\vec{m}_1 \cdot \vec{m}_2}{d_{12}^3}\right)$, with μ_{water} being the permeability of the solution. The van der Waals force ($\vec{F}_{vdw}$) can be calculated by $\vec{F}_{vdw} = -\nabla U_{vdw}$ [33], where U_{vdw} is the van der Waals potential and it can be obtained by $U_{vdw,12} = -\frac{A}{6}\left(\frac{2R^2}{d_{12}^2 - 4R^2} + \frac{2R^2}{d_{12}^2} + ln\frac{d_{12}^2 - 4R^2}{d_{12}^2}\right)$, with A being the Hamaker constant and R the radius of the cluster.

Due to the presence of PAA on the cluster surface, both electrostatic repulsion from surface charges and steric repulsion from the polymer volume were included in the calculations. The deprotonation of carboxyl groups on PAA impart strong negative charges, promoting inter-cluster repulsion. This electrostatic interaction between adjacent clusters is primarily governed by double-layer forces, as described by DLVO theory: $\vec{F_e} = -\nabla U_e$, and $U_e = 2\pi\epsilon_0\epsilon_r R\zeta^2 \ln\left(1 + e^{-\frac{d_{12}-2R}{\kappa^{-1}}}\right)$, where ϵ_0 is the permittivity of free space, ϵ_r the relative permittivity, and ζ the zeta potential [34]. From Figure 2f, ζ is determined to be -41 mV for sample M4. The cluster radius (R) is approximately 30 nm, based on the average size of sample M4 in Figure 3g. The Debye-Hückel length κ^{-1} is calculated using [34]: $\kappa^{-1} = \sqrt{\varepsilon_r\varepsilon_0 k_B T/2000 N_A e^2 I}$, where k_B is Boltzmann constant, T the temperature in kelvins, N_A Avogadro's number, e the elementary charge, and I the ionic strength. The ionic strength for sample M4, estimated from a pure PAA solution at the same pH, is 2.38×10^{-4} mol/L.

The steric repulsion between two adjacent clusters is calculated by $F_s = -\nabla U_s$ [33], where the potential U_s is defined as $U_s = 2\pi R^2 N_s k_B T\left\{2 - \frac{d_{12}-2R}{\delta} - \frac{d_{12}}{\delta}\ln\left(\frac{2R+2\delta}{d_{12}}\right)\right\}$, where δ and N_s represent the thickness of the PAA layer and the surface density of PAA, respectively.

Figure 5c illustrates the simulated force profile as interparticle spacing varies under a 2020 G magnetic field. At 173 nm, the net force reaches zero, indicating the equilibrium position between the two clusters. Spacing below this threshold produces repulsive forces, while larger spacing results in attraction, driving assembly. As the magnetic field decreases from 2020 G to 60 G, the equilibrium spacing expands from 173 nm to 264 nm. As shown in Figure 5d, these theoretical values align closely with Bragg's law and experimental measurements. The model also explains the diffraction behavior: strong fields cause minor peak shifts, whereas weak fields (<500 G) lead to rapid redshifts. The calculations confirm that large inter-cluster gaps—much greater than cluster radius—minimize size variation effects, enabling stable 1D photonic chains with vivid, tunable colors across the visible spectrum.

4. Conclusions

This study demonstrates that magnetic assembly can effectively produce one-dimensional photonic crystals from nonuniform Fe_3O_4 nanocrystal clusters. By leveraging PAA modification to impart strong electrostatic repulsion, large interparticle separations were achieved, mitigating the impact of size polydispersity and enabling periodic structures with tunable optical diffraction across the visible spectrum. Experimental results and force-dynamics modeling confirm that magnetic, electrostatic, van der Waals, and steric interactions collectively govern the assembly behavior, with equilibrium spacing significantly exceeding cluster size. This relaxed requirement for particle uniformity, combined with scalable synthesis and broad spectral tunability, offers a practical route for fabricating responsive photonic materials over large areas. These findings pave the way for cost-effective, magnetically responsive optical devices for sensing, display, and adaptive photonics.

Supplementary Materials: The following supporting information can be downloaded at: https://media.sciltp.com/articles/others/2512261112538084/MI-25120043-Supplementary_Materials.pdf, Figure S1: (a) The photographs of sample M4 during RF fixation; (b) the possibly corresponding assembly behaviors. Figure S2: The observation angle and magnetic field direction in Figure 4a. Figure S3: The reflection peak wavelength and structural color comparison of sample M4 with concentrations of 10 mg/mL and 20 mg/mL upon exposure to magnetic fields.

Author Contributions: Y.Y.: conceptualization, supervision, writing—reviewing and editing; F.Q.: methodology, investigation, data curation, visualization, writing—original draft preparation; Q.F.: simulation, software, validation; C.W.: investigation. All authors have read and agreed to the published version of the manuscript.

Funding: This work was supported by the U.S. National Science Foundation (CHE-2203972).

Data Availability Statement: Data are available from the corresponding author upon reasonable request.

Conflicts of Interest: The authors declare no conflict of interest.

Use of AI and AI-Assisted Technologies: No AI tools were used to prepare this paper.

References

1. Ge, J.; Yin, Y. Responsive photonic crystals. *Angew. Chem. Int. Ed.* **2011**, *50*, 1492–1522.
2. Li, Z.; Yin, Y. Stimuli-Responsive Optical Nanomaterials. *Adv. Mater.* **2019**, *31*, 1807061.
3. Li, Z.; Yang, F.; Yin, Y. Smart materials by nanoscale magnetic assembly. *Adv. Funct. Mater.* **2020**, *30*, 1903467.
4. Hou, J.; Li, M.; Song, Y. Patterned colloidal photonic crystals. *Angew. Chem. Int. Ed.* **2018**, *57*, 2544–2553.
5. Li, F.H.; Tang, B.T.; Wu, S.L.; Zhang, S.F. Facile Synthesis of Monodispersed Polysulfide Spheres for Building Structural Colors with High Color Visibility and Broad Viewing Angle. *Small* **2017**, *13*, 1602565. https://doi.org/10.1002/smll.201602565.

6. Zhang, Y.; Fu, Q.; Ge, J. Test-Paper-Like Photonic Crystal Viscometer. *Small* **2017**, *13*, 1603351. https://doi.org/10.1002/smll.201603351.
7. Hou, K.; Ali, W.; Lv, J.; Guo, J.; Shi, L.; Han, B.; Wang, X.; Tang, Z. Optically Active Inverse Opal Photonic Crystals. *J. Am. Chem. Soc.* **2018**, *140*, 16446–16449. https://doi.org/10.1021/jacs.8b10977.
8. Shang, L.R.; Fu, F.F.; Cheng, Y.; Yu, Y.R.; Wang, J.; Gu, Z.Z.; Zhao, Y.J. Bioinspired Multifunctional Spindle-Knotted Microfibers from Microfluidics. *Small* **2017**, *13*, 1600286. https://doi.org/10.1002/smll.201600286.
9. Fenzl, C.; Hirsch, T.; Wolfbeis, O.S. Photonic Crystals for Chemical Sensing and Biosensing. *Angew. Chem.-Int. Ed.* **2014**, *53*, 3318–3335. https://doi.org/10.1002/anie.201307828.
10. Fu, F.; Chen, Z.; Zhao, Z.; Wang, H.; Shang, L.; Gu, Z.; Zhao, Y. Bio-inspired self-healing structural color hydrogel. *Proc. Natl. Acad. Sci. USA* **2017**, *114*, 5900–5905. https://doi.org/10.1073/pnas.1703616114.
11. Wang, J.; Sultan, U.; Goerlitzer, E.S.A.; Mbah, C.F.; Engel, M.; Vogel, N. Structural Color of Colloidal Clusters as a Tool to Investigate Structure and Dynamics. *Adv. Funct. Mater.* **2019**, *30*, 1907730. https://doi.org/10.1002/adfm.201907730.
12. Lu, W.; Asher, S.A.; Meng, Z.H.; Yan, Z.Q.; Xue, M.; Qiu, L.L.; Yi, D. Visual detection of 2,4,6-trinitrotolune by molecularly imprinted colloidal array photonic crystal. *J. Hazard. Mater.* **2016**, *316*, 87–93. https://doi.org/10.1016/j.jhazmat.2016.05.022.
13. Qin, M.; Huang, Y.; Li, Y.; Su, M.; Chen, B.; Sun, H.; Yong, P.; Ye, C.; Li, F.; Song, Y. A Rainbow Structural-Color Chip for Multisaccharide Recognition. *Angew. Chem.* **2016**, *55*, 6911–6914. https://doi.org/10.1002/anie.201602582.
14. Zhao, Z.; Wang, H.; Shang, L.; Yu, Y.; Fu, F.; Zhao, Y.; Gu, Z. Bioinspired Heterogeneous Structural Color Stripes from Capillaries. *Adv. Mater.* **2017**, *29*, 1704569. https://doi.org/10.1002/adma.201704569.
15. Fu, Q.; Zhu, H.; Ge, J. Electrically Tunable Liquid Photonic Crystals with Large Dielectric Contrast and Highly Saturated Structural Colors. *Adv. Funct. Mater.* **2018**, *28*, 1804628. https://doi.org/10.1002/adfm.201804628.
16. Reese, C.E.; Baltusavich, M.E.; Keim, J.P.; Asher, S.A. Development of an intelligent polymerized crystalline colloidal array colorimetric reagent. *Anal. Chem.* **2001**, *73*, 5038–5042.
17. Ward Muscatello, M.M.; Stunja, L.E.; Thareja, P.; Wang, L.; Bohn, J.J.; Velankar, S.S.; Asher, S.A. Dependence of photonic crystal nanocomposite elasticity on crystalline colloidal array particle size. *Macromolecules* **2009**, *42*, 4403–4406.
18. Ge, J.; Hu, Y.; Yin, Y. Highly tunable superparamagnetic colloidal photonic crystals. *Angew. Chem.* **2007**, *46*, 7428–7431. https://doi.org/10.1002/anie.200701992.
19. Ge, J.; Hu, Y.; Zhang, T.; Huynh, T.; Yin, Y. Self-assembly and field-responsive optical diffractions of superparamagnetic colloids. *Langmuir* **2008**, *24*, 3671–3680. https://doi.org/10.1021/la7039493.
20. Luo, W.; Ma, H.; Mou, F.; Zhu, M.; Yan, J.; Guan, J. Steric-Repulsion-Based Magnetically Responsive Photonic Crystals. *Adv. Mater.* **2014**, *26*, 1058–1064. https://doi.org/10.1002/adma.201304134.
21. Li, Z.; Yin, S.; Cheng, L.; Yang, K.; Li, Y.; Liu, Z. Magnetic targeting enhanced theranostic strategy based on multimodal imaging for selective ablation of cancer. *Adv. Funct. Mater.* **2014**, *24*, 2312–2321.
22. Cheng, C.; Xu, F.; Gu, H. Facile synthesis and morphology evolution of magnetic iron oxide nanoparticles in different polyol processes. *New J. Chem.* **2011**, *35*, 1072–1079. https://doi.org/10.1039/c0nj00986e.
23. Chen, J.; Feng, J.; Li, Z.; Xu, P.; Wang, X.; Yin, W.; Wang, M.; Ge, X.; Yin, Y. Space-Confined Seeded Growth of Black Silver Nanostructures for Solar Steam Generation. *Nano Lett.* **2019**, *19*, 400–407. https://doi.org/10.1021/acs.nanolett.8b04157.
24. Xu, W.; Wang, M.; Li, Z.; Wang, X.; Wang, Y.; Xing, M.; Yin, Y. Chemical Transformation of Colloidal Nanostructures with Morphological Preservation by Surface-Protection with Capping Ligands. *Nano Lett.* **2017**, *17*, 2713–2718. https://doi.org/10.1021/acs.nanolett.7b00758.
25. Ge, J.; Hu, Y.; Biasini, M.; Beyermann, W.P.; Yin, Y. Superparamagnetic Magnetite Colloidal Nanocrystal Clusters. *Angew. Chem. Int. Ed.* **2007**, *46*, 4342–4345. https://doi.org/10.1002/anie.200700197.
26. Das, K.K.; Somasundaran, P. Ultra-low dosage flocculation of alumina using polyacrylic acid. *Colloids Surf. Physicochem. Eng. Asp.* **2001**, *182*, 25–33. https://doi.org/10.1016/S0927-7757(00)00735-4.
27. Liu, L.; Luo, S.-Z.; Wang, B.; Guo, Z. Investigation of small molecular weight poly(acrylic acid) adsorption on γ-alumina. *Appl. Surf. Sci.* **2015**, *345*, 116–121. https://doi.org/10.1016/j.apsusc.2015.03.145.
28. Liu, S.; Ye, Z.; Yin, Y. Seeded Growth of Plasmonic Nanostructures in Deformable Polymer Confinement. *Langmuir* **2024**, *40*, 8760–8770. https://doi.org/10.1021/acs.langmuir.4c00706.
29. Ye, Z.; Tai, Y.; Han, Z.; Liu, S.; Etheridge, M.L.; Pasek-Allen, J.L.; Shastry, C.; Liu, Y.; Li, Z.; Chen, C.; et al. Engineering Magnetic Nanoclusters for Highly Efficient Heating in Radio-Frequency Nanowarming. *Nano Lett.* **2024**, *24*, 4588–4594. https://doi.org/10.1021/acs.nanolett.4c00721.
30. Hu, Y.; He, L.; Yin, Y. Magnetically Responsive Photonic Nanochains. *Angew. Chem.-Int. Ed.* **2011**, *50*, 3747–3750. https://doi.org/10.1002/anie.201100290.

31. Li, Z.; Wang, M.; Zhang, X.; Wang, D.; Xu, W.; Yin, Y. Magnetic Assembly of Nanocubes for Orientation-Dependent Photonic Responses. *Nano Lett.* **2019**, *19*, 6673–6680. https://doi.org/10.1021/acs.nanolett.9b02984.
32. Li, Z.; Liu, Y.; Marin, M.; Yin, Y. Thickness-dependent wrinkling of PDMS films for programmable mechanochromic responses. *Nano Res.* **2020**, *13*, 1882–1888.
33. Xue, X.; Furlani, E.P. Analysis of the Dynamics of Magnetic Core–Shell Nanoparticles and Self-Assembly of Crystalline Superstructures in Gradient Fields. *J. Phys. Chem. C* **2015**, *119*, 5714–5726. https://doi.org/10.1021/jp513025w.
34. Liu, Y.; Han, X.; He, L.; Yin, Y. Thermoresponsive Assembly of Charged Gold Nanoparticles and Their Reversible Tuning of Plasmon Coupling. *Angew. Chem.-Int. Ed.* **2012**, *51*, 6373–6377.